BuyTheDips: PathLoss for improved topology-preserving deep learning-based image segmentation

Minh Ôn Vũ Ngọc[1*], Yizi Chen[1,2*§], Nicolas Boutry[1‡], Jonathan Fabrizio[1] and Clément Mallet[2]
[1] EPITA Research and Development Lab. LRDE, Le Kremlin-Bicêtre, France
[2] Univ. Gustave Eiffel, IGN-ENSG, LaSTIG, Saint-Mandé, France

***Abstract*—Capturing the global topology of an image is essential for proposing an accurate segmentation of its domain. However, most of existing segmentation methods do not preserve the initial topology of the given input, which is detrimental for numerous downstream object-based tasks. This is all the more true for deep learning models which most work at local scales. In this paper, we propose a new topology-preserving deep image segmentation method which relies on a new leakage loss: the Pathloss. Our method is an extension of the BALoss [1], in which we want to improve the leakage detection for better recovering the closeness property of the image segmentation. This loss allows us to correctly localize and fix the critical points (a leakage in the boundaries) that could occur in the predictions, and is based on a shortest-path search algorithm. This way, loss minimization enforces connectivity only where it is necessary and finally provides a good localization of the boundaries of the objects in the image. Moreover, according to our research, our Pathloss learns to preserve stronger elongated structure compared to methods without using topology-preserving loss. Training with our topological loss function, our method outperforms state-of-the-art topology-aware methods on two representative datasets of different natures: Electron Microscopy and Historical Map.**

***Index Terms*—Image segmentation, Topology, Shortest path, Leakage loss**

I. Introduction

IMAGE segmentation is still a challenging task in the field of computer vision and has received a lot of attention during the last few decades [2]–[5]. Image segmentation aims to partition an image into distinct segments, in other words, associate a label to each pixel [6]. In light of the very successful trend toward learning-based image analysis, various methods have been proposed to improve the performance of deep learning-based image segmentation [2], [7]–[10]. Deep-based image segmentation methods can be trained in an end-to-end way and applied to a wide range of problems by learning better image representations compared to handcrafted ones. These methods have focused on either extracting better features from the network or designing more powerful deep architectures to make them more robust to appearance variations. Despite of their high per-pixel accuracy, most of current solutions are still susceptible to make errors when recovering thin connections, fine details of structures, or multiple connected components that share the same contour.

The boundary ground truth is a binary image which embeds strong topology properties between adjacent regions. Therefore, correct segmentation of the boundary is extremely important in case of dense image segmentation [11] and multiple instances [12] for two reasons. First, contour information is frequently shared across neighboring objects in the image. Secondly, location errors or leakages on boundaries of the regions are detrimental for instance retrieval and subsequently in downstream tasks. In biomedical images, for example, correctly segmenting thin objects like membranes plays an important role in providing accurate structure qualification in order to count the right number of instances for diagnosis purposes [13]–[17]. On the other hand, in the case of the historical maps, reliable extraction of the contours of the roads and buildings is required to recover the spatial and semantic information in archival maps [18], [19], mandatory input for subsequent social historical analysis. These topology-related segmentation tasks put emphasis on the utter importance in recovering correct topology connections in the boundary of pixels: the missing detection of such contour pixel might cause failure in topology, especially in the first dimension of topology properties (examples are shown in Fig. 1b and 1c)[1].

To address this issue, several methods have been proposed focusing on refining boundary-aware information on the boundaries of objects [20]–[22]. Although traditional deep-learning based methods have significantly improved pixel level accuracy and contour preservation, the missed detection of key pixels will lead to an incorrect number of segments or instances. To tackle such a problem, Mosinka *et al.* [23] have proposed a deep-learning based solution which can gradually strengthen the continuity of pixels by combining recursive refinement (based on the concept of Lipschitz continuity [23]) and feature consistency properties in VGG [24] networks. Indeed, the topological improvement [23] is proved through an adequate topological evaluation [25] by strengthening the continuity of curvilinear structures in images. However, this method does not utilize any topology-related properties

*Equal contribution
‡Corresponding author.
§This work has been conducted in the context of the SoDuCo project, grant ANR-18-CE38-0013.

[1]Zero topology is related to the number of connected components; one dimension topology is related to a circular hole.

(a) Original image. (b) U-Net output [3]. (c) U-Net result [3]. (d) Our output. (e) Our result.

Fig. 1: An example of the failure case on biomedical image segmentation using U-Net [3] alone and the topological correction by our method. (a) Original image. (b),(c) The boundary prediction and image segmentation of U-Net [3]. (d), (e) The boundary prediction and image segmentation of our proposed method.

which are essential in guaranteeing closed shapes. To provide stronger topology properties in deep image segmentation tasks, Hu *et al.* [11] directly use a topology analysis tool called persistent homology for preserving and refining the missed detection pixels in the boundaries (so-called saddle points). Briefly speaking, this method transfers the likelihood image into a persistent diagram and pairs the persistent dots (also called connected components) in both ground truths and predictions where the topological errors in the predictions are the localized saddle points between the pairwise persistent dots. However, pairing the persistent dots are not always optimal due to the background noise, in particular when the image size and the number of instances are large. Moreover, the computational complexity of persistent homology is cubic to the image size which is difficult to apply in large images.

In order to address the topology-preserving problem and provide a better solution to localize the broken connections in object boundaries, we propose a new loss for deep-based segmentation approaches, named **PathLoss** (*PL*). The goal of PathLoss is to localize and boost up the weak points of boundaries more efficiently. An overview of our method is illustrated in Fig. 3. We treat the edge probability map (an output of the U-Net based [3] architectures) as a landscape and extract all the dips on the ridges of the mountain to localize all leakage positions in the image. Our approach relies on a seeded segmentation approach where each seed is automatically associated with a region in the ground truth image. We leverage the geodesic information for finding the shortest path between the seeds of adjacent regions. Then, the leakage position is defined as the intersection between the shortest path and the boundary of the region. Eventually, we calculate the mean square distance between the value of the broken pixels and ground truth, boosting up the value in the broken edges while training the neural network. Compared to [11], our method can accurately localize leakage pixels efficiently without any intermediate steps.

Our PathLoss (*PL*) is combined with the classical binary cross entropy loss in the training process to further refine the boundary details. The power of our loss relies on the fact that it allows to propagate the boundary information for regulating the network behavior while keeping a similar network structure. Our method is model-agnostic and can be plugged into different network architectures.

To prove that our PathLoss (*PL*) can improve the topological structure in the likelihood image predicted by neural networks, we test *PL* on biomedical images (Electron Microscopy) [26]–[28] and historical map datasets [29]. Examples of the impact of our method on the region boundaries are shown in Fig. 1d and 1e. Especially, the task of segmentation historical maps is crucial for many studies (e.g. social science and historical study) but remain challenging due to limited texture information and many overlaps. By applying Pathloss in historical map segmentation task, the topology perspective of predicted boundaries of objects are significantly improved. The experimental results show that our method outperforms state-of-the-art topology-preserving methods including Mosin [23], Topoloss [30], BALoss [1], clDice [31], and Iternet [32].

Our contributions can be summarized as follows:

- We propose a new leakage loss function (PathLoss), which efficiently localizes critical points in the boundaries of regions.
- Our loss function can maintain strong topology properties and low sensitivity in the likelihood predictions with any segmentation networks. We also visualize the closeness properties of the features.
- Our loss function can be trained efficiently and is insensitive to noise compared to other topology-related loss functions so that no further post-processing steps (such as watershed segmentation approaches) is required.

This paper is organized as follows. The following section lists existing researches including different methods of semantic edge detection and how to improve the topology correctness in the predictions. Then, the geodesic information is recalled in Sec. III which is the foundation of our method. In Sec. IV, our proposed solution is illustrated with insightful details. In Sec. V and Sec. VI, we evaluate our method in different datasets to prove the improvement of topology correctness between ours and state-of-the-art methods. In the last section, we conclude this paper and list the possible future works.

II. Related work

This section introduces and discusses the existing work of semantic edge detection methods, learning inter-pixel correlation, and topology-preserving image segmentation methods.

Semantic edge detection methods: Recently, numerous deep learning methods have been proposed to improve results

in image segmentation tasks [33]–[36]. The multi-scale features which are extracted from Convolutional Neural Networks (CNN) are widely applied [37]–[39] into the detection of semantic edges from images. The learnable module called gated-CRF [38] is used as an attention to encapsulate all convolutional features into a more discriminative representation (similar to sequence learning [40], [41]). It can achieve better fusion quality compared to traditional deep learning-based semantic edge detection methods [42]. However, in topology-related applications, although these methods propose satisfactory per-pixel level accuracy, the false predicted pixels in the boundaries can cause failure of detecting number of objects in the images [11].

Learning pixel connectivity: By considering the image as a graph, maximin affinity learning of image segmentation (MALIS) [43] classifies the connectivity between pixel pairs (also called affinity graph), the threshold affinity graph can be used to form connected components for instance segmentation purposes. However, thresholding is such a simple method for graph partitioning can lead to misclassifications of one or a few edges of the affinity graph. Inspired from the ideas from MALIS [43], Oner et al. [44] first predicted the Euclidean distance map and used an hybrid loss by combining the correctness of the distance map and the pairwise shortest cost between two connected components to improve the connectivity in road segmentation task.

One way to maintain topology properties in the object detection task is to make sure the information of inter-pixel correlations (also called pixel connectivity) is correct. Nowozin et al. [45] proposed a method by learning the parameters of Markov Random Field (MRF) with information of global connectivity to connect pixels of every object. Kampffmeyer et al. [46] proposed a network (connectivity network) for saliency object detection which first encodes and predict the inter-pixel relationships as well as the number of foreground neighboring pixels by using neural networks. Since pixel connectivity has symmetry properties, Yang et al. proposed biconnect [47], which improves the connectivity network by using shared weights between pairwise neighboring pixels (so-called bilateral voting), instead of using independent weights for pair-wise connectivity. Inspired from [46], [47], Chen et al. [48] uses the connectivity network to detect more consistency edges in historical map segmentation task. Alternativey, Jie et al. [49] proposed a spatial attention network that jointly learns the segmentation and connectivity information for road detection to focus on the pixels that are connected to their neighbors. In [50], Yan *et al.* used the graph neural network (GNN) to propagate and aggregate the features of the vertices for regularized road extraction. However, the connectivity network does not guarantee the topology-correctness in the output predictions which is strongly required in historical map segmentation tasks. To conclude, the aforementioned approaches apply information of pixel connectivity (zero-dimensional topology properties) that can boost the performance of object segmentation results, however, it does not guarantee topology properties in one-dimensional topology properties. Note that the one-dimensional topology properties related to closed shape detection (the number of instances for segmentation) is crucial in curvilinear image segmentation task i.e. electron microscopy and historical maps.

Topology-preserving image segmentation methods: Topology-preserving image segmentation methods mainly consist of indirect and direct ways. The indirect way uses an iteration framework to gradually refine the elongated structure in the predicted output, while latter one directly use strong topology priors and constraints to improve topological results in the predictions. The worth noted indirect way stems from Mosinska et al. [23], where a topology-awareness loss is proposed by measuring the similarities of features in VGG-19 [51] between ground truths and predictions. However, this work assumed that the line continuity of trained filters in the VGG-19 can maintain the topology properties in the predicted probability map, albeit it does not have any guarantee of high dimensional topology such as loops (or closed boundaries). Therefore, the detected objects might not be topologically correct. Different from the Mosinka et al. [23] where the predicted likelihood is joined to the image input for refinement purposes, the work in Iternet [32], Multi-stage multi-recursive-input networks [52] and Flood-Filling Networks [53] stack several network to gradually refine the likelihood in each stage of the networks, still, those methods suffer the similar issue.

The direct topology-preserving methods focus on using persistent homology [54] to measure the topology features of image predictions [54]. Chen et al. [55] introduced the topology priors and integrate them into Conditional Random Fields (CRF) image models to improve the image segmentation tasks. Persistent homology has been widely used as a topology feature. Recently, persistent homology has been redesigned and has proved its differentiable properties while it can be used as a topology-preserving loss function and can be applied to any end-to-end deep neural networks [11], [30], [56], [57]. However, the limitations of using persistent homology in deep image segmentation tasks are its memory consumption, convergence speed, and sometimes the training difficulty when combined with other loss functions. In [31], the authors proposed a new topology-awareness metrics to measure the similarity between images based on morphological skeletons. However, clDice still yield missing centerlines on the leakage locations in the prediction image.

Seeded based image segmentation approaches: Cerrone et al. [13] proposed an end-to-end network based on Random Walker algorithms to predict the edge weights. Lei et al. [58] illustrate the concept called Adaptive Morphological Reconstruction (AMR) to improve the seed-based spectral segmentation. Watershed [59] as one of the best seeded image segmentation method can be used to maintain the closed shapes in instance segmentation applications [18], [19]. Wolf *et al.* [60] came up with the idea of the learnable watershed for seeded image segmentation by training an altitude function with region assignment benefit from reinforcement learning [61]. Recently, Minh *et al.* [1] proposed a boundary-awareness loss (BALoss) relying on minimum barrier distance (MBD) which can accurately refine a set of broken edges, eventually improving the segmentation quality in microscopy images. Compared to all methods mentioned above, our Pathloss focuses on the critical points at the topological level, and

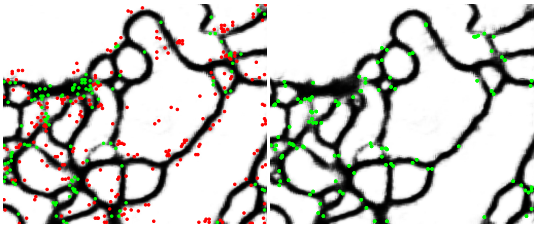

Fig. 2: A comparison between the critical points of Topoloss [11] (left) and our proposed Pathloss (right), the red points are the irrelevant critical points and green critical points are activated during the learning process.

Model	M	TA	Cri-P	Bo-Pi	Cri-P-F
Iternet [32]	IN	✗	✗	✗	–
Mosin [62]	IN+Loss	✗	✗	✗	–
BL [63]	Loss	✗	✗	✓	–
clDice [31]	Loss	✓	✗	✓	–
BALoss [1]	Loss	✓	✗	✓	–
Topoloss [11]	Loss	✓	✓	✓	✗
Pathloss (ours)	Loss	✓	✓	✓	✓

TABLE I: A comparison between our method and state-of-the-art methods: methods use IN (iteration based network) or Loss (topology-preserving loss); TA: The topology aware in the training process of the method; Cri-P: methods use information of critical points or not; Bo-Pi: methods focus on boundary pixels; Cri-P-F: methods do not require to filter the critical points. In this paper, we aim to close more shapes based on the condition of the first dimensional topology and focused on fixing the critical points in the boundary pixels.

achieves better topological accuracy than the state-of-the-art methods (e.g., TopoLoss [11] and BALoss [1]). A comparison between the critical points of the Topoloss [11] and our Pathloss is illustrated in Fig. 2. To summarize the key methods above, we provide a Tab. I for better comparing different topology related methods. Our new loss is an extension of the BALoss [1] to improve the detection of critical pixels.

III. Geodesic distance at a glance

This section recalls the definition of the geodesic distance, a simple but effective method to find the shortest path between two points in the image. Formally, an image is modeled as a 2D function $u : \Omega \to \mathbb{R}$, where Ω is the image domain. The geodesic strength τ of a smooth curve γ between two pixels s, s' in the given image is defined as:

$$\tau(\gamma) = \int \|\dot{\gamma}(t)\|_{\gamma(t)} dt, \tag{1}$$

in which $\dot{\gamma}$ is the *velocity vector* of γ and $\|.\|_{\gamma(t)}$ is a norm (see [64] for more details). Note that the geodesic strength is computed by splitting the integration into pieces where the curve is smooth [65]. From that definition, the geodesic distance $d(s, s')$ between two points s, s' is deduced as the minimum of the geodesic strengths of all the curves between two given points:

$$d(s, s') = \min_{\gamma \in \Pi(s,s')} \tau(\gamma), \tag{2}$$

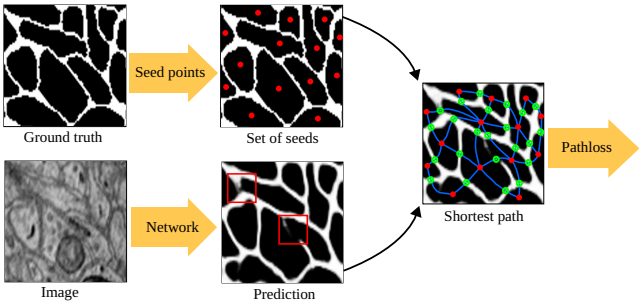

Fig. 3: The pipeline of our method. We first generate the set of seeds (red dots) which correspond to each region in the ground truth image. We then combine the set of seeds and the boundary prediction (the output of the network), to correctly identify the topological errors on the boundaries (red rectangle). To do so, we search for the intersections (green dots) of the boundaries in the ground truth and the shortest paths (blue lines) between red dots in the prediction. These green dots are the critical points, with possible leakages. Then we compute our Pathloss function using these critical points.

where $\Pi(s, s')$ is the set of paths π going from s to s'. In the topographical view, the geodesic distance is computed by considering an image as a landscape. Distances between pixels on the flat terrain are shorter than pixels that have hills and valleys in the heightmap [66].

In discrete form, the image can be modeled as a graph, in which W_{s_i,s_j} represents the weight along the edge $[s_i, s_j]$ on the graph. The geodesic distance on the graph is:

$$d(s, s') = \min_{\pi \in \Pi(s,\, s')} \sum_{s_i \in \pi, i=0}^{N-1} W_{s_i,s_{i+1}}, \tag{3}$$

where $s_0 = s$ and $s_N = s'$. The integration becomes the sum of edge weights along the path connecting s and s'. Then, the geodesic distance is the distance along a path where the accumulation of image gradient reaches the minimum. In a flat zone, the shortest path is similar to the Euclidean distance.

In the next section, we propose to use this distance to recover the shortest path between points in the image, as a basis to compute our Pathloss function.

IV. Proposed method

We present here our method. It relies on a new loss, the Pathloss, to train a deep neural network to correctly segment an image. This loss aims to enforce the activation in the broken connections on the boundaries of the regions. The overview of our method is exposed in Fig. 3. The total loss of the network is defined as $L_{total}(u, g)$ (where u is the predictions and g is the ground truth), which equals the sum of the weighted pixel-level binary cross entropy L_{BCE} and Pathloss L_{PL}:

$$L_{total}(u, g) = L_{BCE}(u, g) + \alpha * L_{PL}(u, g), \tag{4}$$

where the selected hyperparameter α is used to control the trade-off between the two losses. The usage of the L_{BCE} is already efficient to train a deep neural network to segment an image. However, it may lead to leakages on the boundaries.

The idea with the Pathloss is to detect these leakages on the boundaries and to penalize them. We detail in the following subsections how to detect and use these leakages to improve the segmentation.

A. Critical points detection

Algorithm 1: Shortest path computation between two pixels s, s' in the image.

Data: Image U, Point s, s', Geomap D, Parent image par
Result: $\pi(s, s')$
Initiate $Q = \emptyset$; $D(s) = 0$;
$Q.push(s, D(s))$;
$par(s) = s$;
while $!Q.empty$ **do**
  $p = Q.pop()$;
  if $p! = s'$ **then**
    for $n \in N_8(p)$ **do**
      $d =$ *Update distance(n)* (Eq. 3);
      if $d < D(n)$ **then**
        $D(n) = d$;
        $Q.push(n, D(n))$;
        $par(n) = p$;
  else
    $\pi(s, s')$ = Trace back the par relationship;
    return$(\pi(s, s'))$

In order to treat the leakage problem during the learning process of the neural network, we have to correctly locate these points. Our method initiates with considering the likelihood map (the output of the network) as a landscape with mountains and valleys. In this map, a broken connection on the boundary of the region corresponds to a dip on the mountain ridge. The idea of the Pathloss function is inspired by Liebig's law [67] (law of the minimum). This law was first developed in agricultural science. It states that a growth is dictated not by total resources available, but by the scarcest resource (limiting factor). The broken connection can also be called a critical point, which is a pixel that has the weakest value compared to other pixels located in the boundary of the region. If we drop water to the basin, the critical point is the position where water first leaks from one region to its neighbor. Therefore, the values of the critical points relate to the correct topology in the image. By finding these critical points, we are able to capture missing pixels, thereby aiding the network to penalize pixels near these structures using the *PL* function.

We formulate the segmentation problem as follows: given the input image I, we aim to provide a prediction u (output of the network) that is topology equivalent to the ground truth image S. To do that, a set of seed nodes $M = m_1, m_2, ..., m_N$ with $m_i \in S_i$ is provided inside each region S_i in the ground truth image. The inter-segment topology A is defined by the pairwise adjacency relations among all the segments, i.e., $S_i, S_j \in A$ *iff* S_i and S_j are adjacent in segmentation S.

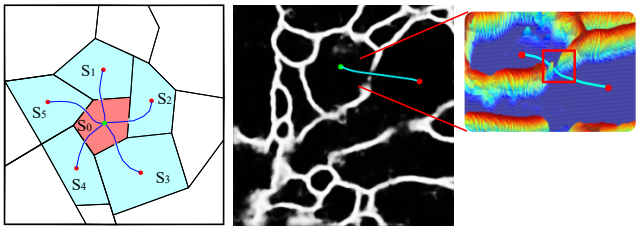

Fig. 4: Leakage (critical points) detection at the intersection of the shortest path and the boundaries of regions.

To preserve the topology of the boundary and measure the quality of segmentation, the shortest path π_{ij} between the pair composed of the seed of m_i and its neighbors m_j is computed using the geodesic distance. The intersection point χ_{ij} between the shortest path π_{ij} and the boundary of the connected component S_i provides the lowest value on the boundary or the weakest edge Fig. 4. These weak points must be enhanced during the learning process to improve the quality of the segmentation.

This is the reason why we must find the shortest path between two regions using the geodesic distance. Such an algorithm is explained in Algo. 1. It is a Dijkstra-like algorithm. We use the 8 adjacency N_8 to define the relationship between neighboring pixel. The propagation procedure is employed by using a priority queue Q. Firstly, the geodesic distance map $D(s)$ and the parent relation $par(s)$ are initiated at the seed pixels. The starting point s is then put into the queue Q. In the next step, we pop out pixels p from the queue Q for the propagation process. Next, we need to update the geodesic distance value D (in Algo. 1) at every neighboring pixel n of p along the path using Eq. 3. For pixels that can be reached from different paths, we select the path that minimizes the distance between the starting point and the current point. We then sort pixels in the queue according to the geodesic distance D. If the updated distance d is lower than its previous value, we update the parent relation par and its new distance value $D(n)$. The process is repeated until the destination point s' is found. The shortest path between two points s, s' is easily traced back using the parent relation par that we updated in the propagation step.

B. Path loss

We present here our method to compute the L_{PL} function. Most CNN-based segmentation networks use binary cross-entropy (BCE) as a loss function. It is defined as a measure of the difference between two probability distributions for a given random variable or set of events [68]. However, BCE does not have the topology property to guarantee a closed boundaries segmentation. Therefore, the L_{PL} function is proposed to enhance the performance of image segmentation. We respectively find the shortest path between each pair of the seed points thanks to the front propagation algorithm. From the shortest path, we deduce critical pixels as the intersection points χ_{ij} of the shortest paths π_{ij} and the object boundaries C_i to find the weakest edge on the boundary. Example of the shortest path is illustrated in Fig. 4. The higher value of the

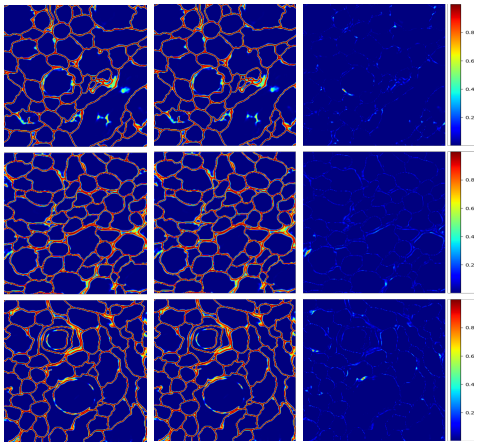

Fig. 5: Three examples of the impact of our Pathloss function on the prediction image. The first column contains the edge probability maps (EPM) at a specific iteration, and the second column contains the EPM at the same iteration but with the contribution of the Pathloss. The third column shows the difference between them. The magnitude of the improvement is illustrated as from blue to red color. We see the improvement on leakages between regions.

intersection point χ_{ij}, the better the segmentation result. The Pathloss L_{PL} is the sum of the Pathloss for every connected component, which is defined as:

$$L_{PL}(u, g) = \sum_{i \in N} \sum_{j \in A(i)} MSE(u(\chi_{ij}), g(\chi_{ij})), \qquad (5)$$

where u and g are respectively the likelihood and ground truth images, N is the number of regions in the ground truth label image.

Our loss function is used to quantize the value of the critical points in the image, thereby evaluating the segmentation quality. A high value of the Pathloss corresponds to many broken connections on the boundary of the connected component. When the loss function L_{PL} is zero, the likelihood of the critical points is 1, i.e., the prediction image is exactly the same as the ground truth image. The advantage of our L_{PL} loss function is that it helps the network to focus on important broken missing pixels on each region, thus preserving the topological structure of the image.

C. Discussion on the Pathloss and training details

We choose to predict edge probability maps instead of labeling the regions to allow our method to handle the relation between neighboring regions in the image. Let call M the binary mask that represents a set of all detected critical pixels, which are intersections between the shortest paths between seed pixels in the image and the region boundaries. It guarantees that all the critical points belong to the ground truth boundary of the image. The set of critical pixels is used to check if there are leakage positions or broken connections on the boundaries. If so, the L_{PL} will force the network to improve the likelihood values on these structures.

We also notice that the edge probability map u will be updated at every epoch. That leads to a re-computation of the shortest path between the neighbor seeds and the critical points. Our method locates the intersection pixels which only depends on u, and the change on the mask M at each epoch is not continuous. This set of critical points is not directly predicted by the network. Therefore, the gradient of L_{PL} exists and can be computed naturally.

Our *PL* function is architecture-agnostic: it can be integrated into any kind of convolutional neural network. In practice, we first pre-train the neural network with only the L_{BCE} to get the global prediction of the edge probability map, and then train the network with the combined loss (binary cross entropy loss + Pathloss). This way provides us more precise intersection pixels of the region boundary, that lead to a better computation of the L_{PL}.

V. Electron Microscopy

We evaluate our proposed method on the challenging task of neuron segmentation in electron microscopy (EM) images [26]–[28].

Datasets. In our experiments, we work on the Electron Microscopy Images from three datasets: ISBI12 [26], ISBI13 [27], and CREMI [28]. The challenge has been designed to measure automated segmentation accuracy in connectomics. The ISBI12 EM Segmentation Challenge [26] is the neuron segmentation challenge that contains 30 images with ground truth annotations of size 512×512. The images are representative of actual images in the real-world, containing some noise and small image alignment errors. ISBI13 dataset [27] consists of 100 images of size 1024×1024. The CREMI dataset [28] is from adult Drosophila melanogaster brain tissue. There are three volumes, and we test on volume A which has 125 slices of size 1250×1250 pixels. This dataset is highly anisotropic and contains artifacts like support film folds, missing sections, and staining precipitations.

Setting. We use a 3-fold cross-validation for the ISBI12, ISBI13, and CREMI datasets. To train the neural network, Adam [69] optimization algorithm is used with a learning rate of 10^{-4}, and an early-stop mechanism to stop the training when the validation loss is no longer decreasing during 15 epochs. Note that α (Eq. 4) is set to a value of 0.1.

Evaluation metrics. We use three complementary metrics to evaluate the performance of our method: ARI, VOI, and CREMI scores [11]. **ARI** is the maximal F-score of the foreground-restricted Rand index (a measure of similarity between two clusters). This version of the Rand index excludes the zero component of the original labels (background pixels of the ground truth). **VOI** is a measure of the distance between two clusterings, closely related to mutual information. It is defined by a sum of the split / merge errors (VOI_s/ VOI_m) which corresponds to over/under-segmentation compared to the ground truth segmentation. **CREMI score** is the geometric mean of **VOI** and adapted RAND error (1-**ARI**).

A. Ablation study on the likelihood prediction

Here we show the impact of our Pathloss based on the improvement between the edge probability map (EPM) with and without the Pathloss. We use the U-Net architecture [3] as

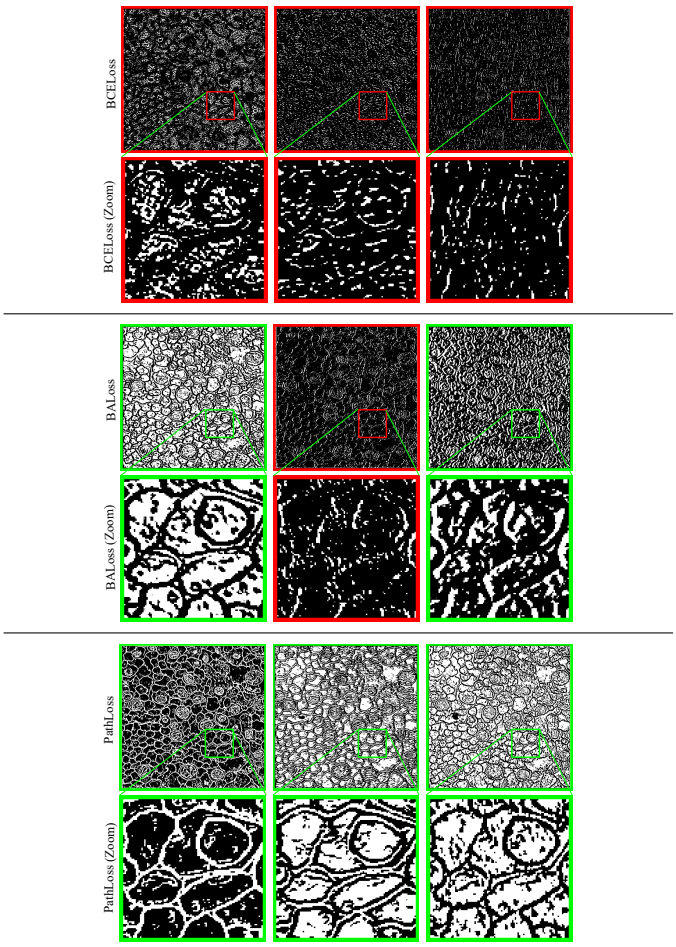

Fig. 6: Feature analysis for different losses of the top-3 weights in the first layer of the networks. The first and second row represent the BCE loss, third and fourth row represent the BALoss, and fifth and sixth row represent the Pathloss. The zoom version of selected regions (boxes in the figures) are shown below the figures. Red: The features show weak elongated structures. Green: The features show strong elongated structures.

	Method	ARI	VOI	CREMI score
ISBI13 dataset	U-Net [3]	0.8913 (±0.015)	1.4973 (±0.091)	0.4034 (±0.091)
	U-Net + PL	**0.9077 (±0.021)**	**1.367 (±0.066)**	**0.347 (±0.042)**
	DC U-Net [70]	0.7913 (±0.031)	1.928 (±0.065)	0.6343 (±0.065)
	DC U-Net + PL	**0.8023 (±0.045)**	**1.7979 (±0.052)**	**0.5962 (±0.052)**
	Nested-U-Net [71]	0.8753 (±0.028)	1.4108 (±0.202)	0.4194 (±0.202)
	Nested-U-Net + PL	**0.8996 (±0.022)**	**1.2665 (±0.152)**	**0.3566 (±0.152)**
ISBI12 dataset	U-Net [3]	0.7669 (±0.019)	1.5005 (±0.126)	0.5914 (±0.126)
	U-Net + PL	**0.8372 (±0.026)**	**1.1973 (±0.107)**	**0.4297 (±0.054)**
	DC U-Net [70]	0.7121 (±0.034)	1.6981 (±0.201)	0.6992 (±0.201)
	DC U-Net +PL	**0.7594 (±0.008)**	**1.5399 (±0.171)**	**0.6087 (±0.171)**
	Nested-U-Net [71]	0.7563 (±0.018)	1.3335 (±0.053)	0.5700 (±0.053)
	Nested-U-Net + PL	**0.8352 (±0.035)**	**1.1808 (±0.270)**	**0.4411 (±0.270)**
CREMI dataset	U-Net [3]	0.9058 (±0.016)	0.7393 (±0.042)	0.2639 (±0.042)
	U-Net + PL	**0.9420 (±0.002)**	**0.6042 (±0.035)**	**0.1852 (±0.009)**
	DC U-Net [70]	0.8288 (±0.010)	1.0470 (±0.042)	0.4234 (±0.042)
	DC-U-Net + PL	**0.9285 (±0.001)**	**0.7019 (±0.023)**	**0.2240 (±0.023)**
	Nested-U-Net [71]	0.9236 (±0.007)	0.4678 (±0.012)	0.1891 (±0.012)
	Nested-U-Net + PL	**0.9420 (±0.003)**	**0.4594 (±0.006)**	**0.1632 (±0.006)**

TABLE II: Improvements brought by the usage of the Pathloss on different network architectures compared the common BCE loss. Best scores are in bold and the standard deviations are provided between brackets.

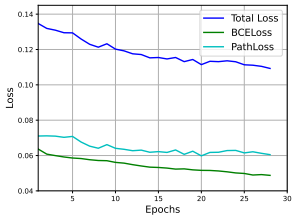

Fig. 7: Loss in terms of training epochs. The Total Loss is the sum of BCELoss and PathLoss. α is equal to 0.1.

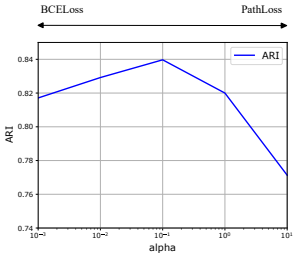

Fig. 8: Impact of α w.r.t. ARI on ISBI12 dataset. When α is 0, the BCEloss is dominating and vice versa. The best score is achieved at α equal 0.1.

the backbone for contour prediction. For the implementation, we respectively predict the EPM with and without the Pathloss from the same initiate weights then compare the difference between these two versions.

The impacts of our proposed loss are illustrated on Fig. 5 for the CREMI dataset [28]. At the first glance, we can see that the improvements concentrate on the edge of the regions, thereby improving the quality of the EPM. It is based on the fact that our Pathloss focuses on detecting critical points on the boundary then penalizes these values. Therefore, it is able to refine the quality of the edge prediction.

B. Feature analysis in Pathloss

Fig. 6 shows the features from different losses BCEloss, BALoss, and Pathloss. We weighted the 3*3 kernels $w_{3\times3}$ of i^{th} kernels of the first layer of U-Net according to:

$$w_i := max|w_{3\times3}|. \quad (6)$$

And we choose the features with the top-3 weights of the ranked 3×3 kernels.

We can see that the features of U-Net trained with BCEloss and BALoss visualize in weak features consistency; while the PathLoss focuses on the critical boundary pixels which lead to a strong sign of feature consistency in the curve structure.

C. Impact of the loss weight α and the training process

We investigate the impact of the value of α on the training process and performances of our method. Our loss function is a weighted combination between the binary cross-entropy and the Pathloss function by the value of α shown in Fig. 7. We choose the value of α equal 0.1. We can see that all the losses decrease in the training process and the Pathloss becomes stable after 20 epochs.

Fig. 8 shows the study of α on the ISBI12 dataset w.r.t *ARI* index. We investigate the values of α on a large range from 0.001 to 10. A small value of α means we only use BCE loss,

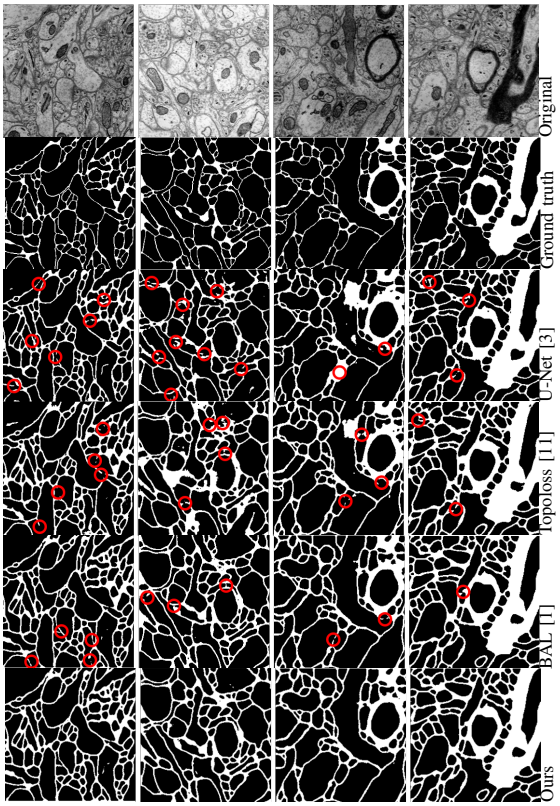

Fig. 9: Qualitative results of our proposed method compared to state-of-the-art methods. Topological errors are shown in the red circles.

	Method	ARI	VOI	CREMI score
ISBI13 dataset	Mosin [23]	0.7504 (±0.040)	1.5018 (±0.137)	0.6122 (±0.137)
	Iternet [32]	0.8686 (±0.001)	1.58556 (±0.141)	0.4564 (±0.141)
	clDice [31]	0.8942 (±0.020)	1.2851 (±0.119)	0.3687 (±0.049)
	U-Net [3]	0.8913 (±0.014)	1.4973 (±0.091)	0.4043 (±0.091)
	U-Net + BL [63]	0.8772 (±0.104)	1.4849 (±0.470)	0.4270 (±0.368)
	Topoloss [11]	0.8864 (±0.026)	1.4623 (±0.049)	0.4076 (±0.049)
	U-Net + BAL [1]	0.9023 (±0.023)	1.3761 (±0.075)	0.3666 (±0.075)
	Ours	**0.9077 (±0.021)**	**1.3671 (±0.066)**	**0.3472 (±0.042)**
ISBI12 dataset	Mosin [23]	0.7833 (±0.012)	1.1332 (±0.079)	0.4955 (±0.079)
	Iternet [32]	0.751 (±0.037)	1.4614 (±0.133)	0.6032 (±0.133)
	clDice [31]	0.7454 (±0.056)	1.6035 (±0.257)	0.6389 (±0.049)
	U-Net [3]	0.7669 (±0.019)	1.5005 (±0.126)	0.5914 (±0.126)
	U-Net + BL [63]	0.8227 (±0.033)	1.1622 (±0.206)	0.4539 (±0.164)
	Topoloss [11]	0.8297 (±0.024)	1.3338 (±0.186)	0.4766 (±0.186)
	U-Net + BAL [1]	0.8138 (±0.019)	**1.0557 (±0.025)**	0.4433 (±0.029)
	Ours	**0.8372 (±0.026)**	1.1973 (±0.107)	**0.4297 (±0.054)**
CREMI dataset	Mosin [23]	0.9185 (±0.012)	0.6278 (±0.043)	0.2262 (±0.043)
	Iternet [32]	0.9240 (±0.039)	0.7147 (±0.020)	0.2330 (±0.020)
	clDice [31]	0.8941 (±0.006)	0.6144 (±0.055)	0.2551 (±0.019)
	U-Net [3]	0.9059 (±0.016)	0.7393 (±0.042)	0.2638 (±0.042)
	U-Net + BL [63]	0.9420 (±0.028)	0.6365 (±0.054)	0.1921 (±0.048)
	Topoloss [11]	0.9257 (±0.001)	0.8021 (±0.016)	0.2441 (±0.016)
	U-Net + BAL [1]	0.9366(±0.006)	0.6893 (±0.010)	0.2090 (±0.010)
	Ours	**0.9420 (±0.002)**	**0.6042 (±0.035)**	**0.1852 (±0.009)**

TABLE III: A comparison of the segmentation performance between our method and state-of-the-art methods on ISBI13, ISBI12 and CREMI datasets. Best scores are in bold and the standard deviations are provided inside brackets.

and vice versa. The value of *ARI* first increases but decreases later as we increase the value of α. When the value of α is too big, the Pathloss dominates the BCE loss and it may enforce the network to overtrain on certain leakage positions on boundaries of regions. Therefore, it may sacrifice global information. We observe that α equal to 0.1 provides the best performance in the microscopy image segmentation task.

D. Ablation study on the networks

In this section, we demonstrate the usefulness of our loss function which is applicable to any kind of convolutional neural network. We exploit the loss function on three different architectures: U-Net [3], DC U-Net [70], and Nested U-Net [71]. DC U-Net and Nested U-Net are chosen because they are the important variant of the U-Net and these experiments prove that the Pathloss is generalized with different models. We first pretrain the U-Net model using the BCE loss to get the best weights, and then train the network with the combined loss. For evaluation, we use pixel accuracy, ARI, VOI, and CREMI scores.

Tab.II shows the quantitative results for three different neuron image datasets. The PathLoss function archives the highest segmentation results in terms of the three topology-aware metrics (ARI, VOI, and CREMI scores). The PathLoss improves maximally 0.0997, 0.3451 and 0.1617 in ARI, VOI and CREMI scores among three different datasets. By using the PathLoss, the performance consistently improves within different architectures, and it proves that our Pathloss can be used in a plug-and-play fashion in different architecture settings to improve the topology correctness in the image segmentation task.

E. Comparison with state-of-the-Art methods

We compare our method with several state-of-the-art segmentation models, including U-Net [3], Mosin [23], Iternet [32], and different topology preserving loss function, Topoloss [11], clDice [31], Boundary loss [63], and BAloss [1] on the same three datasets.

Qualitative analysis Fig. 9 shows the qualitative results of our method compared with state-of-the-art methods. At the first glance, we can see that our method outperforms other methods for preserving the topology of the images. Our loss function is able to penalize the broken connections, which are depicted as the red regions in Fig. 9, to close some contour regions in the image, thereby increasing the number of segmented regions compared to the ground truth image. As a consequence, the quality of the contour likelihood is improved during the training process. Our method demonstrates more consistency in terms of structures and topology and is able to correctly segments fine structures. However, our method may create some small noises in the regions, which can be easily removed using some simple post-processing methods.

Quantitative analysis The quantitative results are provided in Tab. III. Note that the better a method, the lower VOI/CREMI scores values, and the higher ARI values. The results are highlighted when they are significantly better. Our

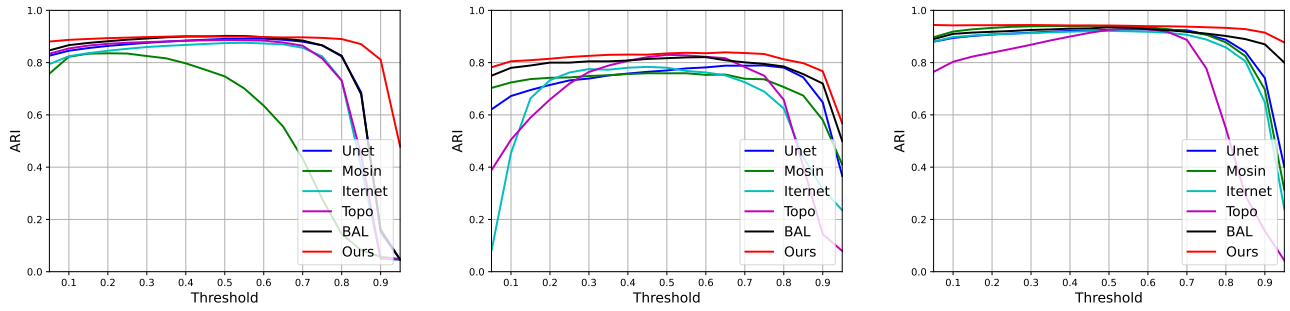

(a) ARI-ISBI13. (b) ARI-ISBI12. (c) ARI-CREMI.

Fig. 10: ARI curves across all the thresholds on ISBI12, ISBI13, CREMI datasets using the Nested-U-Net as the backbone. Our Pathloss is stable and achieves the best score compared to other methods over all the thresholds.

Pathloss achieves the best performance in ARI and CREMI scores, while it is comparable in VOI score compared to U-Net+BAL [1] and Mosinka [23]. In ISBI13 dataset, our PathLoss improves 0.5%, 0.0009 and 0.0194 in ARI, VOI and CREMI scores compared to the second-best performance in BALoss [1]. Similarly, in CREMI score, PathLoss improves 0.5%, 0.0851 and 0.0238 in ARI, VOI and CREMI scores (with respect to the BALoss). In ISBI12 dataset, PathLoss improves 2% and 0.0136 in ARI and CREMI scores but decreases 0.1416 in VOI score compared to BALoss.

To evaluate the stability of our proposed method, for each image, we simply binarize the corresponding EPM with a threshold sliding from 0.05 to 0.95. Then, for every threshold, we compare the obtained binary map with the ground-truth map. In Fig. 10, we show the ARI curves for varying thresholds of the prediction EPM. If we look at the ARI curves, there are two main observations. First, our method has stable/flat curves, which is an advantage, because the "best" threshold remains unknown and depends on the image. Conversely, for the other methods (namely U-Net, Mosin, Iternet, and Topoloss), the curves are not stable, which means that taking a threshold might not be a very robust task. The second observation is that our method gets better results than these state-of-the-art methods on all the thresholds.

VI. Historical Map Segmentation

In this section, we experiment with our method for the specific application of segmenting historical maps. This task consists in detecting a set of closed shapes (building blocks) in digitized historical maps for tracking long-term human changes. In the 18th century, the massive development of topographic maps at various scales, and in particular city maps has allowed to document the partitioning of the territories and now to foster information extraction from such sources for automatic spatio-temporal dynamic retrieval. These maps describe the distribution of space which contains rich, detailed, and numerous geographical entities with geometrically accurate representations embedded with semantic information. Recovering the spatial and semantic information in old maps requires a so-called *vectorization* process [48]. In particular, vectorizing maps consists in transforming the rasterized graphical representation in a vectorized one. Then these geographic

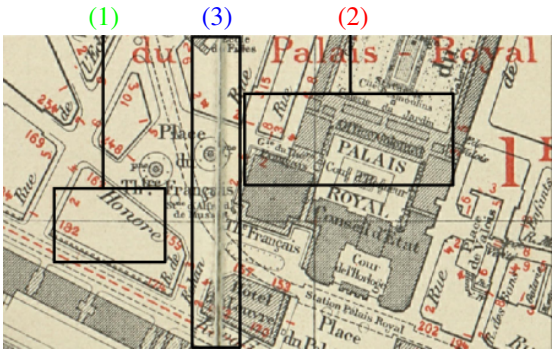

Fig. 11: Challenges in historical maps: (1) planimetric overlap, (2) text overlap, (3) paper fold.

entities are converted into instance geographic data, that can be subsequently manipulated by using Geographic Information System (GIS).

Unfortunately, the characteristics of historical maps hinder standard pattern recognition approaches which fail extracting correct instances. First, historical maps have an issue called planimetric overlap. It means texture and non-textural objects overlap, which creates ambiguities in the detection of objects (see Fig 11(1)). Occlusion (Fig 11(2)) is another issue where texts and carto-geodetic information are overlaid: map objects are partially hidden. It makes it difficult to distinguish objects in historical maps even for humans. Moreover, paper folds or holes (Fig 11(3)) can create artifacts such as gaps in the cartographic information that will make objects split into two. An example of the failure case in the historical map is shown in Fig. 12.

Dataset. The historical map dataset is taken from the challenge detailed here [29]. The images of the dataset are composed of two maps from Paris atlases ("*Atlas municipal des Vingt arrondissements de Paris*"), in the years 1898 and 1926. The map from the year 1926 is split into two continuous regions that are used for training and validation, where the training part has 3,343 objects with 4,500×9,000 pixels, while the validation part has 3,000×9,000 pixels with 2,183 objects. The testing image is chosen from the year 1898, which has 6,500×5,500 pixels with 2,836 objects.

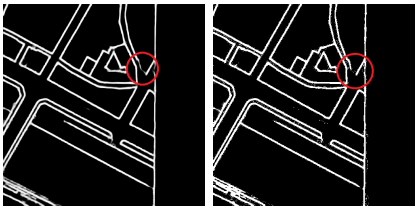

Fig. 12: Connected component extraction (**CC labelling**): we threshold the edge probability map and run connected component analysis to get instances from the images. The red circle shows a weak boundary that disappears after threshold.

Backbone. In this experiment, we use U-Net [3] architecture as our backbone for evaluating the performance of our Pathloss function.

Setting. During the training phase, we use the following settings: ADAM optimizer with an initial learning rate of 10^{-4}, a momentum of 0.9, and a weight decay of 0.002. An early-stopping mechanism is used to stop the training when the validation loss is no longer decreasing in 15 epochs range.

Evaluation metrics. To evaluate our results, we use a customized **COCO** panoptic evaluation matrix [72], designed specifically for historical maps [73]. The correctnesses of detected objects are measured through the Intersection over Unions (*IoU*) between predicted and ground truth instances. We calculate COCO panoptic scores as follows. First, for each pair of shapes (t_i, p_j) in the target and in the predicted segmentations, the Jaccard index (or *IoU*) is computed as

$$IoU(t_i, p_j) = \frac{t_i \cap p_j}{t_i \cup p_j}. \tag{7}$$

Then, the set of uniquely matching pairs (or *true positives*) TP is defined as the set of all pairs (t_i, p_j) such as $IoU(t_i, p_j) > 0.5$, leading to the definition of PQ:

$$PQ = \frac{\sum_{(t_i,p_j)\in TP} IoU(t_i, p_j)}{|TP| + \frac{1}{2}|FP| + \frac{1}{2}|FN|}, \tag{8}$$

where FP is the set of *false positives* (the set of *predicted* shapes which do not belong to any pair TP), and FN is the set of *false negatives* (the set of *target* shapes which do not belong to any pair in TP). While this measure summarizes the segmentation and the detection quality into a single indicator, two additional metrics provide additional insights: the Segmentation Quality (SQ) and the Recognition Quality (RQ) defined such as $PQ = SQ \times RQ$ where:

$$SQ = \frac{\sum_{(t_i,p_j)\in TP} IoU(t_i,p_j)}{|TP|}, \quad RQ = \frac{|TP|}{|TP|+\frac{1}{2}|FP|+\frac{1}{2}|FN|}$$

Baselines. We use the results of the paper [48] as our baseline. Firstly, the HED [42], BDCN [39] and U-Net [3] models are used to predict EPMs of object boundaries, and instances are extracted through connected components. Then, the watershed image segmentation method is used as a post-processing step [19], [48] to recover more closed shapes compared to connected component methods. We also tested two topology-preserving methods Mosin [23], Topoloss [11] and BALoss [1] on recovering weak edges to compare to our approach. These three losses are well-known as the function of preserving topology in image segmentation, and it is also used in the application of electron microscopy.

Method	Validation			Test		
	PQ	SQ	RQ	PQ	SQ	RQ
U-Net	34.8	80.5	43.3	8.1	78.2	10.4
HED	23.2	76.5	30.3	14.0	74.8	18.8
BDCN	27.7	80.6	34.4	10.2	80.4	12.7
U-Net +WS	56.6	87.7	64.5	18.3	85.2	21.4
HED + WS	50.5	87.2	57.9	35.6	84.6	42.0
BDCN + WS	52.5	87.8	59.8	34.9	85.8	40.6
Mosin	68.2	86.2	79.0	34.1	84.5	40.3
Topoloss	70.0	**88.5**	79.1	36.7	**86.4**	42.4
BALoss	63.3	85.2	74.3	39.9	83.1	48.0
Ours	**70.7**	88.3	**80.1**	**40.0**	85.5	**46.8**

TABLE IV: Quantitative results for different models on the historical dataset. Best scores are in bold. The *WS* represents watershed post-processing methods used for closed shape extraction from EPMs.

Quantitative analysis. We compare the four different deep learning architectures, HED [37], BDCN [39], Mosinka [23] and U-Net [3] combined with different loss functions. Their performances are illustrated in Tab. IV. The first observation from Tab. IV is that **the existing deep learning architectures with topology refinement can significantly increase the performance of instance segmentation results in historical map applications.** As we could see from Tab. IV, the Mosinka [23] and Topoloss [11] steadily increase the metrics: 19.5% and 18.4% in COCO PQ score compared to two-step methods (using watershed as post-processing), in validation and testing dataset respectively. The advantage of using the topology refining method is that it does not require any post-processing or extra steps to find the best parameter setting (e.g., area and dynamic in watershed image segmentation). Moreover, our PathLoss has a better performance in COCO PQ compared to [11], [23] with a better COCO RQ score. The better RQ implies that the background noise of predictions in our PathLoss is lower. The second observation is that **the PathLoss loss provides good generalization compared to both watershed image segmentation and baseline topology refining approaches.** The paper [48] uses the watershed post-processing step (WS) to extract more closed shapes in the EPMs. Compared to the best performance in [48] (HED+WS), our PathLoss significantly improves 20.2% and 4.4% in validation and testing datasets without applying watershed post-processing steps. About the topology-preserving loss functions, the baselines based on topology refinement [11], [23] achieve satisfactory results in the validation set, the performances in the testing set is significantly lower, where our PathLoss can still maintain the best performance in both validation and testing datasets. Tab. IV shows that Pathloss improves 0.7% and 3.3% in both validation and testing datasets, where the testing dataset is chosen from year 1898 which is different from training and validation datasets (from year 1925) for the purposes of testing the generalization of different models. In conclusion, our PathLoss effectively localizes and activates the weak edges in images to achieve the best

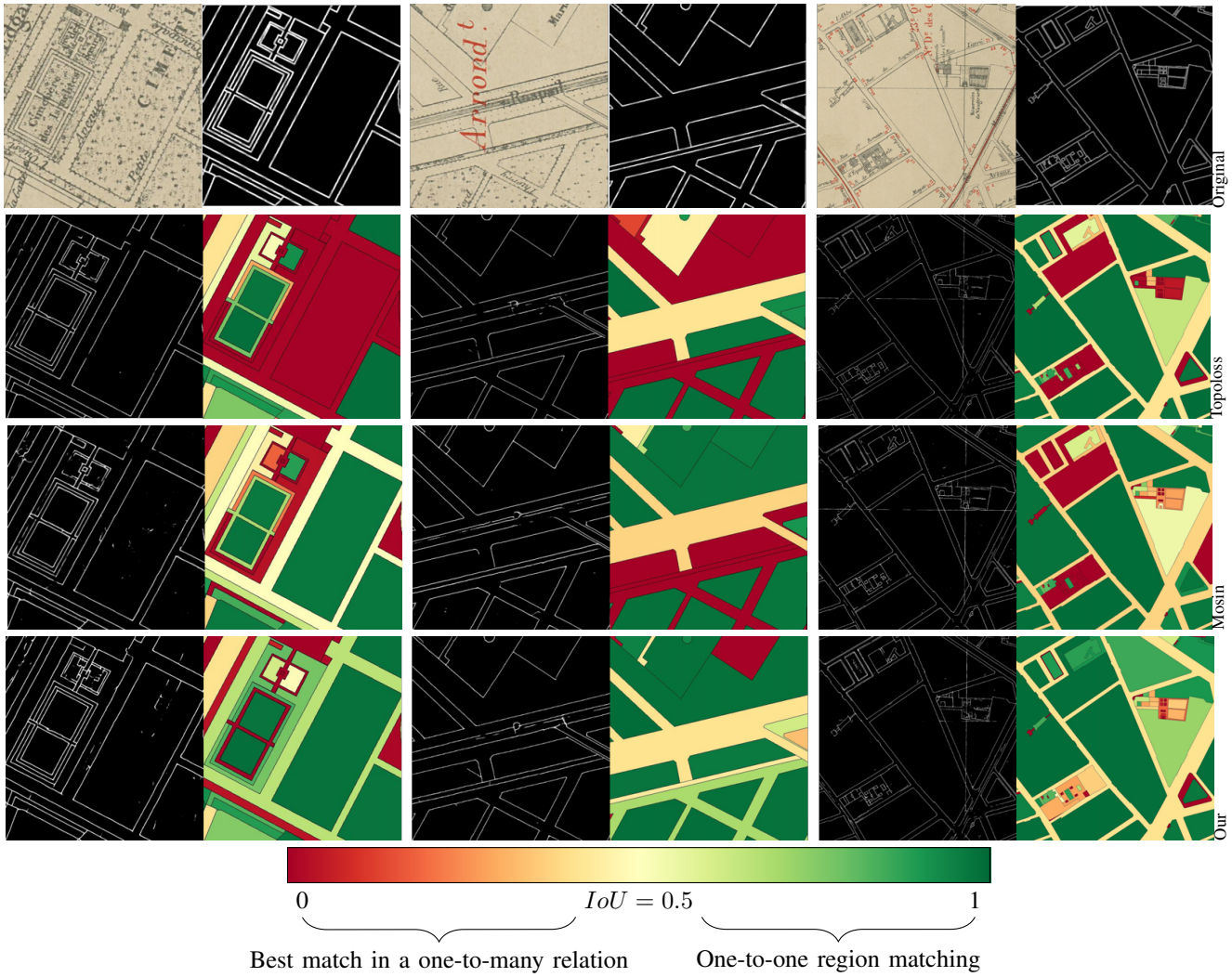

Fig. 13: Qualitative results of our proposed method compared to state-of-the-art methods. The first/second of each example respectively corresponds to the edge probability map (EPM) and the recall map of each method. The scale IoU from bad to good segmentation is illustrated as from red to green color.

performance in the validation dataset while still maintaining satisfactory generalization in the testing dataset.

Qualitative analysis. The qualitative results of three different topology-preserving techniques are shown in Fig. 13. The first/second row in each example respectively shows the edge prediction map (EPM) and the recall map for each method. At the first glance, we can see that even a small break connection on the EPM can significantly damage the structure of the image, which is depicted as the red region in the recall map. The Pathloss function is able to identify and penalize topological errors on the prediction image to maintain the closeness property. As a consequence, our proposed method outperforms the Topoloss and Mosin methods to recover more correct objects on the historical map.

VII. Conclusions

In this paper, we proposed a new loss function (so-called PathLoss) to maintain as much as possible the structure of the image. Different with state-of-the-art methods, our seed-based segmentation approach efficiently localizes critical points in the boundary of objects by using the geodesic shortest path algorithm. Indeed, our method successfully extends the BALoss [1] for recovering the closeness property of the image segmentation. Our Pathloss is able to penalize the leakages between the neighboring objects to preserve the first dimensional topological structure in the deep image segmentation task. We have also investigated the impact of the proposed loss function on the feature maps to prove its strong consistency property. The PathLoss is capable to gradually refine the broken connections to recover more correct object regions, thereby outperforming state-of-the-art methods in ISBI12, ISBI13, CREMI and Historical map datasets. Moreover, the PathLoss can be used in a plug-and-play fashion with different architecture settings to gradually improve and preserve topology structure in image segmentation tasks. The perspective of our work is to apply this loss function to improve the perceptual edge detection in the natural, satellite and biomedical images. As a matter of reproducible research, the source code of our method

is available at https://github.com/onvungocminh/PathLoss.

REFERENCES

[1] M. Ô. V. Ngoc, Y. Chen, N. Boutry, J. Chazalon, E. Carlinet, J. Fabrizio, C. Mallet, and T. Géraud, "Introducing the boundary-aware loss for deep image segmentation," in *British Machine Vision Conference (BMVC) 2021*, 2021.

[2] J. Long, E. Shelhamer, and T. Darrell, "Fully convolutional networks for semantic segmentation," in *Proceedings of the IEEE/CVF Conference on Computer Vision and Pattern Recognition*, 2015, pp. 3431–3440.

[3] O. Ronneberger, P. Fischer, and T. Brox, "U-Net: Convolutional networks for biomedical image segmentation," in *International Conference on Medical Image Computing and Computer-Assisted Intervention*. Springer, 2015, pp. 234–241.

[4] H. Noh, S. Hong, and B. Han, "Learning deconvolution network for semantic segmentation," in *Proceedings of the IEEE/CVF International Conference on Computer Vision*, 2015, pp. 1520–1528.

[5] Y. Pang, Y. Li, J. Shen, and L. Shao, "Towards bridging semantic gap to improve semantic segmentation," in *Proceedings of the IEEE/CVF International Conference on Computer Vision*, 2019, pp. 4230–4239.

[6] M. Bai and R. Urtasun, "Deep watershed transform for instance segmentation," in *Proceedings of the IEEE/CVF Conference on Computer Vision and Pattern Recognition*, 2017, pp. 5221–5229.

[7] M. Tan and Q. Le, "Efficientnet: Rethinking model scaling for convolutional neural networks," in *International Conference on Machine Learning*. PMLR, 2019, pp. 6105–6114.

[8] V. Mnih and G. E. Hinton, "Learning to label aerial images from noisy data," in *Proceedings of the 29th International Conference on Machine Learning (ICML-12)*, 2012, pp. 567–574.

[9] L.-C. Chen, Y. Zhu, G. Papandreou, F. Schroff, and H. Adam, "Encoder-decoder with atrous separable convolution for semantic image segmentation," in *Proceedings of the European conference on computer vision (ECCV)*, 2018, pp. 801–818.

[10] H. Ding, X. Jiang, B. Shuai, A. Q. Liu, and G. Wang, "Context contrasted feature and gated multi-scale aggregation for scene segmentation," in *Proceedings of the IEEE Conference on Computer Vision and Pattern Recognition*, 2018, pp. 2393–2402.

[11] X. Hu, L. Fuxin, D. Samaras, and C. Chen, "Topology-preserving deep image segmentation," *arXiv preprint arXiv:1906.05404*, 2019.

[12] L. Porzi, S. R. Bulo, and P. Kontschieder, "Improving panoptic segmentation at all scales," in *Proceedings of the IEEE/CVF Conference on Computer Vision and Pattern Recognition*, 2021, pp. 7302–7311.

[13] L. Cerrone, A. Zeilmann, and F. A. Hamprecht, "End-to-end learned random walker for seeded image segmentation," in *Proceedings of the IEEE/CVF Conference on Computer Vision and Pattern Recognition*, 2019, pp. 12 559–12 568.

[14] J. Funke, F. Tschopp, W. Grisaitis, A. Sheridan, C. Singh, S. Saalfeld, and S. C. Turaga, "Large scale image segmentation with structured loss based deep learning for connectome reconstruction," *IEEE Transactions on Pattern Analysis and Machine Intelligence*, vol. 41, no. 7, pp. 1669–1680, 2018.

[15] A. Bailoni, C. Pape, S. Wolf, A. Kreshuk, and F. A. Hamprecht, "Proposal-free volumetric instance segmentation from latent single-instance masks," in *Pattern Recognition: 42nd DAGM German Conference, DAGM GCPR 2020, Tübingen, Germany, September 28–October 1, 2020, Proceedings 42*. Springer, 2021, pp. 331–344.

[16] S. Wolf, A. Bailoni, C. Pape, N. Rahaman, A. Kreshuk, U. Köthe, and F. A. Hamprecht, "The mutex watershed and its objective: Efficient, parameter-free graph partitioning," *IEEE Transactions on Pattern Analysis and Machine Intelligence*, pp. 1–1, 2020.

[17] S. Wolf, Y. Li, C. Pape, A. Bailoni, A. Kreshuk, and F. A. Hamprecht, "The semantic mutex watershed for efficient bottom-up semantic instance segmentation," in *European Conference on Computer Vision*, 2020, pp. 208–224.

[18] Y. Chen, E. Carlinet, J. Chazalon, C. Mallet, B. Dumenieu, and J. Perret, "Vectorization of historical maps using deep edge filtering and closed shape extraction," in *16th International Conference on Document Analysis and Recognition (ICDAR'21)*, 2021.

[19] Y. Chen, E. Carlinet, J. Chazalon, C. Mallet, B. Duménieu, and J. Perret, "Combining deep learning and mathematical morphology for historical map segmentation," in *International Conference on Discrete Geometry and Mathematical Morphology*. Springer, 2021, pp. 79–92.

[20] G. Bertasius, J. Shi, and L. Torresani, "Semantic segmentation with boundary neural fields," in *Proceedings of the IEEE/CVF Conference on Computer Vision and Pattern Recognition*, 2016, pp. 3602–3610.

[21] L.-C. Chen, J. T. Barron, G. Papandreou, K. Murphy, and A. L. Yuille, "Semantic image segmentation with task-specific edge detection using cnns and a discriminatively trained domain transform," in *Proceedings of the IEEE/CVF Conference on Computer Vision and Pattern Recognition*, 2016, pp. 4545–4554.

[22] H. Ding, X. Jiang, A. Q. Liu, N. M. Thalmann, and G. Wang, "Boundary-aware feature propagation for scene segmentation," in *Proceedings of the IEEE/CVF International Conference on Computer Vision*, 2019, pp. 6819–6829.

[23] A. Mosinska, P. Marquez-Neila, M. Koziński, and P. Fua, "Beyond the pixel-wise loss for topology-aware delineation," in *Proceedings of the IEEE/CVF Conference on Computer Vision and Pattern Recognition*, 2018, pp. 3136–3145.

[24] K. Simonyan and A. Zisserman, "Very deep convolutional networks for large-scale image recognition," in *3rd International Conference on Learning Representations, ICLR 2015, San Diego, CA, USA, May 7-9, 2015, Conference Track Proceedings*, Y. Bengio and Y. LeCun, Eds., 2015. [Online]. Available: http://arxiv.org/abs/1409.1556

[25] J. D. Wegner, J. A. Montoya-Zegarra, and K. Schindler, "A higher-order crf model for road network extraction," in *Proceedings of the IEEE/CVF Conference on Computer Vision and Pattern Recognition*, 2013, pp. 1698–1705.

[26] I. Arganda-Carreras, S. C. Turaga, D. R. Berger, D. Cireşan, A. Giusti, L. M. Gambardella, J. Schmidhuber, D. Laptev, S. Dwivedi, J. M. Buhmann *et al.*, "Crowdsourcing the creation of image segmentation algorithms for connectomics," *Frontiers in Neuroanatomy*, vol. 9, p. 142, 2015.

[27] I. Arganda-Carreras, H. Seung, A. Vishwanathan, and D. Berger, "3d segmentation of neurites in em images challenge," in *International Symposium on BIOMEDICAL IMAGING*, 2013.

[28] CREMI, "Miccai challenge on circuit reconstruction from electron microscopy images," *https://cremi.org*, 2017.

[29] J. Chazalon, E. Carlinet, Y. Chen, J. Perret, B. Duménieu, C. Mallet, T. Géraud, V. Nguyen, N. Nguyen, J. Baloun, L. Lenc, , and P. Král, "Icdar 2021 competition on historical map segmentation," in *Proceedings of the 16th International Conference on Document Analysis and Recognition (ICDAR'21)*, Lausanne, Switzerland, 2021.

[30] X. Hu, Y. Wang, L. Fuxin, D. Samaras, and C. Chen, "Topology-aware segmentation using discrete morse theory," *arXiv preprint arXiv:2103.09992*, 2021.

[31] S. Shit, J. C. Paetzold, A. Sekuboyina, I. Ezhov, A. Unger, A. Zhylka, J. P. Pluim, U. Bauer, and B. H. Menze, "cldice-a novel topology-preserving loss function for tubular structure segmentation," in *Proceedings of the IEEE/CVF Conference on Computer Vision and Pattern Recognition*, 2021, pp. 16 560–16 569.

[32] L. Li, M. Verma, Y. Nakashima, H. Nagahara, and R. Kawasaki, "Iternet: Retinal image segmentation utilizing structural redundancy in vessel networks," in *Proceedings of the IEEE/CVF Winter Conference on Applications of Computer Vision*, 2020, pp. 3656–3665.

[33] P. Pinheiro and R. Collobert, "Recurrent convolutional neural networks for scene labeling," in *International Conference on Machine Learning*. PMLR, 2014, pp. 82–90.

[34] D. Eigen and R. Fergus, "Predicting depth, surface normals and semantic labels with a common multi-scale convolutional architecture," in *Proceedings of the IEEE International Conference on Computer Vision*, 2015, pp. 2650–2658.

[35] L.-C. Chen, G. Papandreou, I. Kokkinos, K. Murphy, and A. L. Yuille, "Deeplab: Semantic image segmentation with deep convolutional nets, atrous convolution, and fully connected crfs," *IEEE Transactions on Pattern Analysis and Machine Intelligence*, vol. 40, no. 4, pp. 834–848, 2017.

[36] H. Zhao, J. Shi, X. Qi, X. Wang, and J. Jia, "Pyramid scene parsing network," in *Proceedings of the IEEE/CVF Conference on Computer Vision and Pattern Recognition*, 2017, pp. 2881–2890.

[37] S. Xie and Z. Tu, "Holistically-nested edge detection," in *Proceedings of the IEEE/CVF International Conference on Computer Vision*, 2015, pp. 1395–1403.

[38] Y. Liu, M.-M. Cheng, X. Hu, K. Wang, and X. Bai, "Richer convolutional features for edge detection," in *Proceedings of the IEEE/CVF Conference on Computer Vision and Pattern Recognition*, 2017, pp. 3000–3009.

[39] J. He, S. Zhang, M. Yang, Y. Shan, and T. Huang, "Bdcn: Bi-directional cascade network for perceptual edge detection," *IEEE Transactions on Pattern Analysis and Machine Intelligence*, 2020.

[40] F. A. Gers, N. N. Schraudolph, and J. Schmidhuber, "Learning precise timing with lstm recurrent networks," *Journal of Machine Learning Research*, vol. 3, no. Aug, pp. 115–143, 2002.

[41] J. Chung, C. Gulcehre, K. Cho, and Y. Bengio, "Empirical evaluation of gated recurrent neural networks on sequence modeling," *arXiv preprint arXiv:1412.3555*, 2014.

[42] S. Xie and Z. Tu, "Holistically-nested edge detection," in *Proceedings of the IEEE/CVF International Conference on Computer Vision*, 2015, pp. 1395–1403.

[43] S. C. Turaga, K. L. Briggman, M. Helmstaedter, W. Denk, and H. S. Seung, "Maximin affinity learning of image segmentation," *arXiv preprint arXiv:0911.5372*, 2009.

[44] D. Oner, M. Koziński, L. Citraro, N. C. Dadap, A. G. Konings, and P. Fua, "Promoting connectivity of network-like structures by enforcing region separation," *arXiv preprint arXiv:2009.07011*, 2020.

[45] S. Nowozin and C. H. Lampert, "Global connectivity potentials for random field models," in *Proceedings of the IEEE/CVF Conference on Computer Vision and Pattern Recognition*. IEEE, 2009, pp. 818–825.

[46] M. Kampffmeyer, N. Dong, X. Liang, Y. Zhang, and E. P. Xing, "Connnet: A long-range relation-aware pixel-connectivity network for salient segmentation," *IEEE Transactions on Image Processing*, vol. 28, no. 5, pp. 2518–2529, 2018.

[47] Z. Yang, S. Soltanian-Zadeh, and S. Farsiu, "Biconnet: An edge-preserved connectivity-based approach for salient object detection," *arXiv preprint arXiv:2103.00334*, 2021.

[48] Y. Chen, E. Carlinet, J. Chazalon, C. Mallet, B. Duménieu, and J. Perret, "Vectorization of historical maps using deep edge filtering and closed shape extraction," in *Proceedings of the 16th International Conference on Document Analysis and Recognition (ICDAR'21)*, Lausanne, Switzerland, Sep. 2021, to appear.

[49] J. Mei, R.-J. Li, W. Gao, and M.-M. Cheng, "Coanet: Connectivity attention network for road extraction from satellite imagery," *IEEE Transactions on Image Processing*, vol. 30, pp. 8540–8552, 2021.

[50] J. Yan, S. Ji, and Y. Wei, "A combination of convolutional and graph neural networks for regularized road surface extraction," *IEEE Transactions on Geoscience and Remote Sensing*, vol. 60, pp. 1–13, 2022.

[51] K. Simonyan and A. Zisserman, "Very deep convolutional networks for large-scale image recognition," *arXiv preprint arXiv:1409.1556*, 2014.

[52] W. Shen, B. Wang, Y. Jiang, Y. Wang, and A. Yuille, "Multi-stage multi-recursive-input fully convolutional networks for neuronal boundary detection," in *Proceedings of the IEEE/CVF International Conference on Computer Vision*, 2017, pp. 2391–2400.

[53] M. Januszewski, J. Maitin-Shepard, P. Li, J. Kornfeld, W. Denk, and V. Jain, "Flood-filling networks," *arXiv preprint arXiv:1611.00421*, 2016.

[54] A. Zomorodian and G. Carlsson, "Computing persistent homology," *Discrete & Computational Geometry*, vol. 33, no. 2, pp. 249–274, 2005.

[55] C. Chen, D. Freedman, and C. H. Lampert, "Enforcing topological constraints in random field image segmentation," in *Proceedings of the IEEE/CVF Conference on Computer Vision and Pattern Recognition*. IEEE, 2011, pp. 2089–2096.

[56] J. R. Clough, N. Byrne, I. Oksuz, V. A. Zimmer, J. A. Schnabel, and A. P. King, "A topological loss function for deep-learning based image segmentation using persistent homology," *arXiv preprint arXiv:1910.01877*, 2019.

[57] F. Wang, H. Liu, D. Samaras, and C. Chen, "Topogan: A topology-aware generative adversarial network," in *European Conference on Computer Vision*. Springer, 2020, pp. 118–136.

[58] T. Lei, X. Jia, T. Liu, S. Liu, H. Meng, and A. K. Nandi, "Adaptive morphological reconstruction for seeded image segmentation," *IEEE Transactions on Image Processing*, vol. 28, no. 11, pp. 5510–5523, 2019.

[59] M. Couprie and G. Bertrand, "Topological gray-scale watershed transformation," in *Vision Geometry VI*, vol. 3168. International Society for Optics and Photonics, 1997, pp. 136–146.

[60] S. Wolf, L. Schott, U. Kothe, and F. Hamprecht, "Learned watershed: End-to-end learning of seeded segmentation," in *Proceedings of the IEEE/CVF International Conference on Computer Vision*, Oct 2017.

[61] R. S. Sutton and A. G. Barto, *Reinforcement learning: An introduction*. MIT press, 2018.

[62] A. Mosinska, P. Marquez-Neila, M. Koziński, and P. Fua, "Beyond the pixel-wise loss for topology-aware delineation," in *Proceedings of the IEEE/CVF Conference on Computer Vision and Pattern Recognition*, 2018, pp. 3136–3145.

[63] H. Kervadec, J. Bouchtiba, C. Desrosiers, E. Granger, J. Dolz, and I. B. Ayed, "Boundary loss for highly unbalanced segmentation," in *International Conference on Medical Imaging with Deep Learning*. PMLR, 2019, pp. 285–296.

[64] S. Sommer, T. Fletcher, and X. Pennec, "Introduction to differential and Riemannian geometry," in *Riemannian Geometric Statistics in Medical Image Analysis*. Elsevier, 2020, pp. 3–37.

[65] G. Peyré, M. Péchaud, R. Keriven, and L. D. Cohen, *Geodesic methods in computer vision and graphics*. Now publishers Inc, 2010.

[66] P. J. Toivanen, "New geodosic distance transforms for gray-scale images," *Pattern Recognition Letters*, vol. 17, no. 5, pp. 437–450, 1996.

[67] H. De Baar, "von liebig's law of the minimum and plankton ecology (1899–1991)," *Progress in Oceanography*, vol. 33, no. 4, pp. 347–386, 1994.

[68] S. Jadon, "A survey of loss functions for semantic segmentation," in *IEEE Conference on Computational Intelligence in Bioinformatics and Computational Biology*. IEEE, 2020, pp. 1–7.

[69] D. P. Kingma and J. Ba, "Adam: A method for stochastic optimization," *arXiv preprint arXiv:1412.6980*, 2014.

[70] A. Lou, S. Guan, and M. H. Loew, "Dc-unet: rethinking the u-net architecture with dual channel efficient cnn for medical image segmentation," in *Medical Imaging 2021: Image Processing*, vol. 11596. International Society for Optics and Photonics, 2021, p. 115962T.

[71] Z. Zhou, M. M. R. Siddiquee, N. Tajbakhsh, and J. Liang, "Unet++: A nested U-Net architecture for medical image segmentation," in *Deep learning in medical image analysis and multimodal learning for clinical decision support*. Springer, 2018, pp. 3–11.

[72] A. Kirillov, K. He, R. Girshick, C. Rother, and P. Dollár, "Panoptic segmentation," in *Proceedings of the IEEE/CVF Conference on Computer Vision and Pattern Recognition*, 2019, pp. 9404–9413.

[73] J. Chazalon and E. Carlinet, "Revisiting the coco panoptic metric to enable visual and qualitative analysis of historical map instance segmentation," in *16th International Conference on Document Analysis and Recognition (ICDAR)*, 2021.